MATERIALS SCIENCE

Bioinspired polymeric woods

Zhi-Long Yu[1]*, Ning Yang[1]*, Li-Chuan Zhou[2], Zhi-Yuan Ma[1], Yin-Bo Zhu[2], Yu-Yang Lu[2], Bing Qin[1], Wei-Yi Xing[3], Tao Ma[1], Si-Cheng Li[1], Huai-Ling Gao[1], Heng-An Wu[2], Shu-Hong Yu[1]†

Woods provide bioinspiration for engineering materials due to their superior mechanical performance. We demonstrate a novel strategy for large-scale fabrication of a family of bioinspired polymeric woods with similar polyphenol matrix materials, wood-like cellular microstructures, and outstanding comprehensive performance by a self-assembly and thermocuring process of traditional resins. In contrast to natural woods, polymeric woods demonstrate comparable mechanical properties (a compressive yield strength of up to 45 MPa), preferable corrosion resistance to acid with no decrease in mechanical properties, and much better thermal insulation (as low as ~21 mW m^{-1} K^{-1}) and fire retardancy. These bioinspired polymeric woods even stand out from other engineering materials such as cellular ceramic materials and aerogel-like materials in terms of specific strength and thermal insulation properties. The present strategy provides a new possibility for mass production of a series of high-performance biomimetic engineering materials with hierarchical cellular microstructures and remarkable multifunctionality.

INTRODUCTION

Nature has been a source of bioinspiration for materials scientists in the design of high-performance engineering materials (*1*–*4*). Wood, as one of the most common natural materials, has attracted enormous attention due to its lightweight and high-strength properties. A thorough analysis of wood structures and an understanding of structure-function relationships are very enlightening to engineering (*5*, *6*). The unique hierarchical cellular structure and matrix (lignin and hemicelluloses) embedded with well-oriented cellulose fibrils endow the wood with admirable mechanical properties. Wood grows by a biologically controlled bottom-up self-assembly, and every structural level contributes to the remarkable properties of wood, including the mechanical properties as well as the multifunctional and adaptive properties (*7*).

As understanding of wood structure merits deep consideration, many wood-inspired advanced materials have been designed using "top-down" or "bottom-up" strategies. Recently, various wood-derived composite materials with amazing performances are fabricated by modifying the microstructure of the natural woods such as the amazing "super wood" or combining wood-derived cellulose with synthetic materials (*8*–*10*). The wood-derived materials have intrinsic outstanding advantages, such as renewability, biodegradability, excellent toughness, and the possibility for novel functionalities (*10*). The low-cost and abundant raw materials also provide a sufficient source for the high-performance wood-derived materials with promising applications. However, it is still a challenge for wood-derived materials to overcome the drawbacks of wood, such as inflammability and poor corrosion resistance.

A bottom-up strategy is another possible route for fabrication of wood-like monoliths by using polymer as the matrix and micro- or nanoscale materials as the building blocks, such as freeze-casting and three-dimensional (3D) printing (*11*). However, the traditional wood-like materials including cellular polymer materials and cellular ceramic materials are limited by the unsatisfactory mechanical performances and poor controllability (*12*, *13*). Most ceramic-based, wood-like materials are made using ceramic powders, followed by an ultrahigh-temperature sintering usually above 1500°C to integrate the powders into a full monolith (*14*–*16*). 3D printing is also an alternative strategy to fabricate cellular materials or inerratic honeycomb structures; however, it is still a challenge to make macroscopic bulks with micrometer-sized structures (*12*).

Here, inspired by wood, we report a new approach for bulk synthesis of a family of artificial polymeric woods with lifelike appearance and cellular structures by the low-temperature curing of predesigned polymeric matrices (Fig. 1, A to D). This time-efficient strategy contrasts strikingly with the decades or hundreds of years needed to grow natural wood. Our artificial woods exhibit not only good controllability in microstructures but also comparable mechanical properties with those of natural wood. Further, in contrast to natural wood, they demonstrate preferable corrosion resistance to humidity and acid with no decrease in mechanical properties, as well as much better thermal insulation (as low as ~21 mW m^{-1} K^{-1}) and fire retardancy. The polymeric woods stand out even from other engineering materials such as cellular ceramic materials and aerogel-like materials in terms of specific strength and thermal insulation properties. They show promise for use as novel biomimetic engineering materials and an alternative to the natural wood.

RESULTS

Material synthesis and characterization

As a matrix substance of natural wood, lignin is a kind of amorphous polyphenol without a well-defined primary structure and can be described as a "chemical web," which glues cellulose fibrils (fig. S1A) (*17*). Resol, a kind of water-soluble liquid phenol-formaldehyde resin (PF) with a similar amorphous polyphenol structure, is used as the substitute matrix (Fig. 1B and fig. S1B). The artificial polymeric wood

[1]Division of Nanomaterials and Chemistry, Hefei National Research Center for Physical Sciences at the Microscale, Chinese Academy of Sciences (CAS) Center for Excellence in Nanoscience, Hefei Science Center of CAS, Collaborative Innovation Center of Suzhou Nano Science and Technology, Department of Chemistry, University of Science and Technology of China, Hefei 230026, China. [2]CAS Key Laboratory of Mechanical Behavior and Design of Materials, Department of Modern Mechanics, CAS Center for Excellence in Complex System Mechanics, University of Science and Technology of China, Hefei 230027, China. [3]State Key Laboratory of Fire Science, University of Science and Technology of China, Hefei 230026, China.
*These authors contributed equally to this work.
†Corresponding author. Email: shyu@ustc.edu.cn

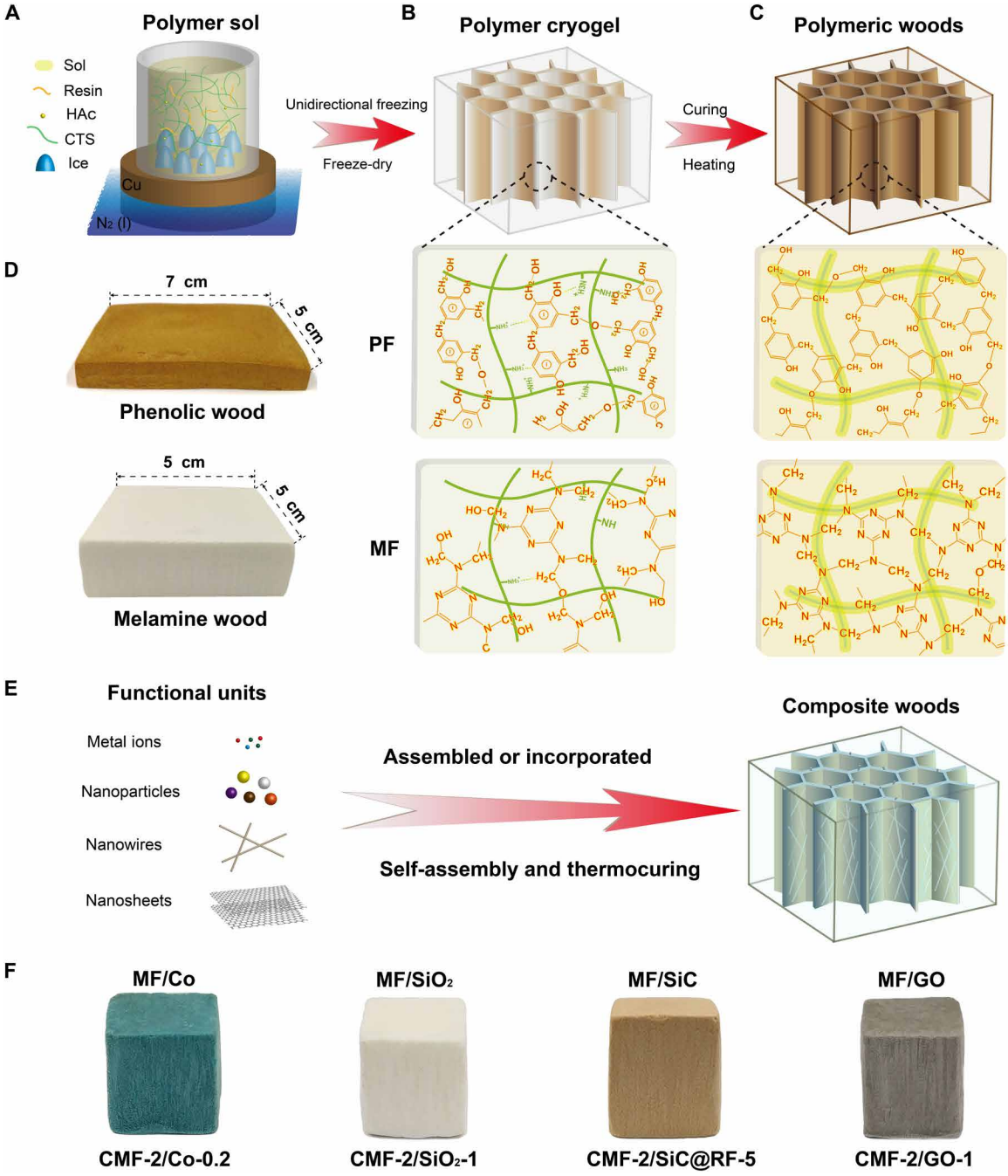

Fig. 1. Fabrication scheme of the bioinspired polymeric woods and kinds of composite woods based on PF and MF. (**A**) Starting solution (sol) including water-soluble thermoset resins, CTS, and acetic acid (HAc), forming a homogeneous polymer solution. (**B**) Predesigned matrix prepared by the ice template–induced self-assembly and freeze-drying process. (**C**) Final polymeric woods after thermocuring the predesigned matrix. The resins are completely cross-linked. (**D**) Photographs of the artificial polymeric woods based on phenolic resin (top, cellular CPF-4-5) and melamine resin (bottom, CMF-3-5). (**E**) Scheme illustration showing the fabrication of various composite woods by adding ions or functional nanomaterials into the polymer solution, followed by the above self-assembly and thermocuring process. (**F**) Photographs of various composite woods based on melamine resin, including MF/Co (CMF-2/Co-0.2), MF/SiO_2 (CMF-2/SiO_2-1), MF/SiC (CMF-2/SiC@RF-5), and MF/GO (CMF-2/GO-1). Size of the composite woods, ~1 cm × 1 cm × 1 cm.

is fabricated by curing the predesigned resin matrix. The hierarchical cellular structures are generated by a unidirectional ice crystal–induced self-assembly process. A small quantity of chitosan (CTS) plays a key role as a temporary scaffold to support the cellular structure and overcome the resins' creep deformation after ice sublimation by means of the strong interaction between the amino groups and the hydroxymethyl groups (*18*). The water-soluble melamine-formaldehyde resin (MF) is also a good matrix candidate due to its countless hydroxymethyls (Fig. 1B and fig. S1C). The polymeric PF- and MF-based woods with perfect cellular structures are completed by a subsequent

curing process at temperatures not higher than 200°C (Fig. 1, C and D). Besides, due to good compatibility, the present approach for polymeric woods provides a new and powerful route to fabricate multifunctional composite cellular materials, and almost all the water-soluble molecules or water-dispersed nanomaterials, such as metal ions, nanoparticles, nanowires, and nanosheets, can be assembled or incorporated into the polymeric woods to form composite woods with different appearances and properties (Fig. 1, E and F). The prepared cellular polymeric woods are named CPF-x_1-y or CMF-x_2-y, where x_1 = 1 to 5 and x_2 = 1 to 3 correspond to the incremental resin content in the solution (table S1), and y corresponds to the freezing rate. For instance, CPF-1-5 and CPF-4-5 are representative of the cellular PF wood prepared by using 3.6 weight % (wt %) and 14.5 wt % resol slurry, respectively, at a freezing rate of 5°C min^{-1}. The composite woods are labeled as CPF-x/Filler-z and CMF-x/Filler-z, where z denotes the concentration (in milligrams per milliliter for nanomaterials and in moles per milliliter for ions or micromolecules) of fillers in the solution.

Wood, such as balsa, consists of parallel hollow tubes with a cell size of about 50 μm and a wall thickness of about 1 μm (Fig. 2, A to C). By using the amorphous PF resin and MF resin as the matrix, we successfully made the macroscopic CPF and CMF woods. As demonstrated by scanning electron microscopy (SEM) images of the cross section and longitudinal section, the typical CPF wood consists of parallel hollow tubes with a pore size of ~50 μm and a wall thickness of 3 to 5 μm (Fig. 2, D to F). The macroscopic CMF wood can also be fabricated with 30- to 40-μm parallel tubes (Fig. 2, G and H). The CMF wood (CMF-3-5) exhibits unique fishbone structures with interconnected channels (Fig. 2I). The fishbone morphology results from the side branches due to the secondary instability formation perpendicular to the freezing direction when the viscous MF polymers concentrate around the primary solid ice cell (*19*). The multifunctionality of the polymeric woods can be realized by compositing functional nanomaterials such as graphene oxide (GO) to the polymer solution (Fig. 2J). The PF/GO composite wood (CPF-1/GO-1) with a low density of ~85 mg cm^{-3} manifests a pore size of ~50 μm and a wall thickness of ~2 μm, and GO is tightly attached to the walls (Fig. 2, K and L). X-ray microtomography of a typical CPF-4-5 revealed the flawless cellular structures with tubes parallel to the freezing direction throughout the material (Fig. 2M and movie S1).

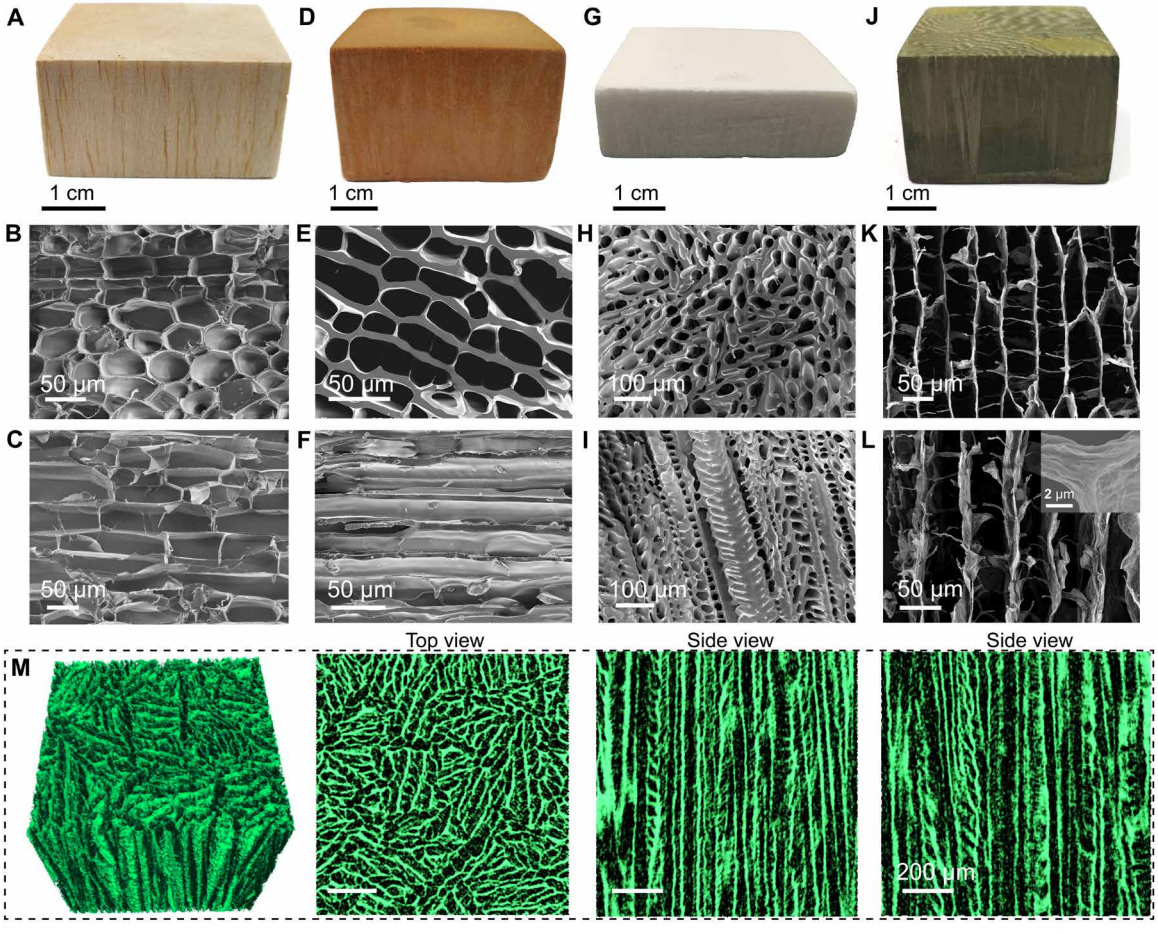

Fig. 2. The structural characterization of the balsa and polymeric woods. (**A**) Balsa wood with a density of ~90 mg cm^{-3}. (**B** and **C**) SEM images of the cross section (perpendicular to the channel direction) and the longitudinal section (parallel to the channel direction) of the balsa wood. (**D**) Artificial CPF wood (CPF-4-5) with a density of ~280 mg cm^{-3}. (**E** and **F**) SEM images of the cross section and the longitudinal section of the CPF wood. (**G**) Artificial CMF wood (CMF-3-5) with a density of ~560 mg cm^{-3}. (**H** and **I**) SEM images of the cross section and the longitudinal section of the CMF wood. (**J**) PF/GO composite wood (CPF-1/GO-1) with a density of ~85 mg cm^{-3}. (**K** and **L**) SEM images of the cross section and the longitudinal section of the PF/GO composite wood. The inset in (L) shows the enlarged image of the node of the walls. (**M**) 3D reconstruction of the CPF wood (CPF-4-5) derived from x-ray microtomography, and microtomography images display the straight, parallel tubular pores. Sale bars, 200 μm.

As to the composite woods, the resin serves as a glue to assemble nanomaterials together, with the fillers dispersed homogeneously in the final cellular materials, leading to diverse visual characteristics and homogeneous microstructures (fig. S2). Besides, large-scale fabrication with different sizes for all these kinds of polymeric woods can be easily achieved due to the cost-effective raw materials and the simple fabrication process (Fig. 1, D to F, and fig. S3).

The pore size and the wall thickness of natural woods are affected by many factors, such as wood species and climate. The cellular structures created by ice templating can also be tuned by parameters such as polymer concentration, freezing rate, and curing temperature. To accurately control the freezing rate, we designed a homemade instrument with a temperature controller (fig. S4). The channel size strongly depends on the resin content and the freezing rate. A slow freezing rate allows the formation of larger pores by the large ice crystals, and a fast freezing rate results in smaller channels because the supercooling impedes the formation of large ice crystals (*20*). In addition, high polymer concentration promotes the formation of small ice crystals and vice versa (*20*, *21*). In correspondence with the above rules, the pores become smaller and the walls become thicker as the resol content increases or the freezing rate increases (fig. S5). To quantitatively assess pore size and wall thickness changes, we determined the statistical area and wall thickness distributions based on the cross-section images. A faster freezing rate and a higher resol content allow narrower distributions of both the pore size and the wall thickness (figs. S6 and S7). The uncontrollable shrinkage of polymer cryogels during the curing process also slightly influences the pore structures and wall thicknesses (figs. S8 to S10). As the freezing rate increases from 1 to 10°C min^{-1}, the average pore size (area) of all CPF samples decreases sharply from 3000 to 6000 μm^2 to 500 to 2000 μm^2, and the average wall thickness decreases from 4 to 8 μm to 1 to 5 μm (fig. S11, A and B), while the curing temperature shows a slight influence on pore size and wall thickness (fig. S11, C and D). Similarly, a faster freezing rate and a higher polymer concentration create smaller pores for CMF woods with obvious fishbone structure due to the high viscosity of the MF solution (fig. S12). Unless stated otherwise, we fabricated polymeric and composite woods at a freezing rate of 5°C min^{-1} and curing at 180°C. In this manner, a family of polymeric woods can be fabricated with well-controlled apparent densities (90 to 600 mg cm^{-3}) and porosities (40 to 90%) (fig. S13).

Mechanical performances and failure mechanism

The low density and high strength of natural woods are the most fascinating advantages that attract considerable research attention. Two kinds of polymeric woods manifest very high compressive strength and elastic modulus along the axial direction due to the anisotropically honeycomb-like microstructures, for example, the compressive yield strengths of CPF-5-10 and CMF-3-5 can achieve ~35 and ~45 MPa and the elastic moduli achieve ~700 and ~653 MPa, respectively (Fig. 3A). Most engineered cellular materials show a scaling relationship of $\sigma/\sigma_s \sim (\rho/\rho_s)^n$ between yield strength (σ) and density (ρ) and $E/E_s \sim (\rho/\rho_s)^n$ between Young's modulus (E) and density, where σ_s, E_s, and ρ_s denote the strength, modulus, and density of the corresponding solid constituent material, respectively (*22*). The power n of the scaling relationship depends on the material microarchitecture. For example, cellular materials with stochastic porosity exhibit the relative elastic modulus scaling with $n = 2$ or 3 (*22*). In general, the honeycombs are very strong and stiff when loaded in the out-of-plane compression (axial direction) (*16*). The linear elastic regime is truncated by structural buckling, and the materials finally failed by tearing or crushing. The relative strength and modulus for an ideal honeycomb structure with regular hexagons and uniform wall thickness, which follow the plastic buckling, scale as $\sigma/\sigma_s \sim (\rho/\rho_s)^2$ and $E/E_s \sim \rho/\rho_s$ from the analytic prediction (*23*). Under axial compression loading, the relative yield strength and relative modulus of CPF materials display approximately quadratic scaling relationships: $\sigma/\sigma_s \sim (\rho/\rho_s)^{2.1}$ and $E/E_s \sim (\rho/\rho_s)^{1.8}$ (Fig. 3B), demonstrating an open-cell structural bending fracture–dominated behavior, where the fracture happens predominantly through the failure of cell walls (*22*). Such a deviation from the theoretical prediction can be explained by defects and structural imperfections. The power n of scaling law between the yield strength and density, as well as the compressive modulus and density of the polymeric woods, was affected by the freezing rate and curing temperature (figs. S14 to S16) in experiments. A faster freezing rate creates more compact and regular structures, resulting in higher strengths and moduli. High temperature facilitates highly cross-linked resin networks, thus generating higher modulus. The irregular polymeric woods with incompletely cured walls prepared by slow freezing rate (1°C min^{-1}) and low curing temperature (160°C) exhibit high scaling power of the elastic modulus ($n \approx 2$). In general, for the relatively regular polymeric woods (freezing rate, >1°C min^{-1}) with completely cured walls (curing temperature, >160°C), the yield strength of the polymeric woods varies approximately as ρ^2, while the Young's modulus varies approximately as $\rho^{1.6}$, demonstrating a bending-dominated failure mode of open-cell structures (Fig. 3C and fig. S17).

Cellular materials always exhibit outstanding compressive performances along the channel direction. The compressive performance of polymeric woods in the axial direction is better than that of ceramic-based wood-like materials such as SiC foams and mullite-zirconia foams as well as the 3D-printed honeycombs (Fig. 3C). The wider density range of the polymeric woods than other engineered wood-like materials manifests a better controllability in the microstructure; that is, the properties can be tuned by different preparation conditions. Besides, the polymeric woods are even comparable to the natural woods in axial-direction compression (Fig. 3C). The elastic moduli of the polymeric woods are much higher than those of corks and the isotropous phenolic aerogels (fig. S17) (*24*, *25*). The elastic moduli are comparable to those of the cellular ceramic materials but are lower than those of natural woods. The oriented crystalline cellulose nanofibers (CNFs) in the natural woods are responsible for the high stiffness. Other materials with stochastic structures such as resorcinol-formaldehyde resin (RF) aerogels and foams usually exhibit a steeper scaling of $E \sim \rho^3$ due to the inefficient load transfer and structural instability in the compression. By contrast, the scaling relationship ($E \sim \rho^{1.6}$) of the polymeric woods manifests more robust cellular structure and improved mechanical efficiency. The compressive property of the polymeric woods in the radial direction is also examined (fig. S18). The radial compressive strengths of the polymeric woods are much higher than those of the common natural woods (Fig. 3C). Besides, the polymeric woods can adsorb modest impact energy due to the slight elasticity in the radial direction, for example, CPF-1 can recover from a 20% compressive strain (fig. S18, D to F). Therefore, polymeric woods can also be used in packaging and protective padding to absorb the kinetic energy without generating intolerably high force on the protected object (*26*).

During axial compression, the balsa wood usually deforms through the cell wall's plastic bending and then reaches densification

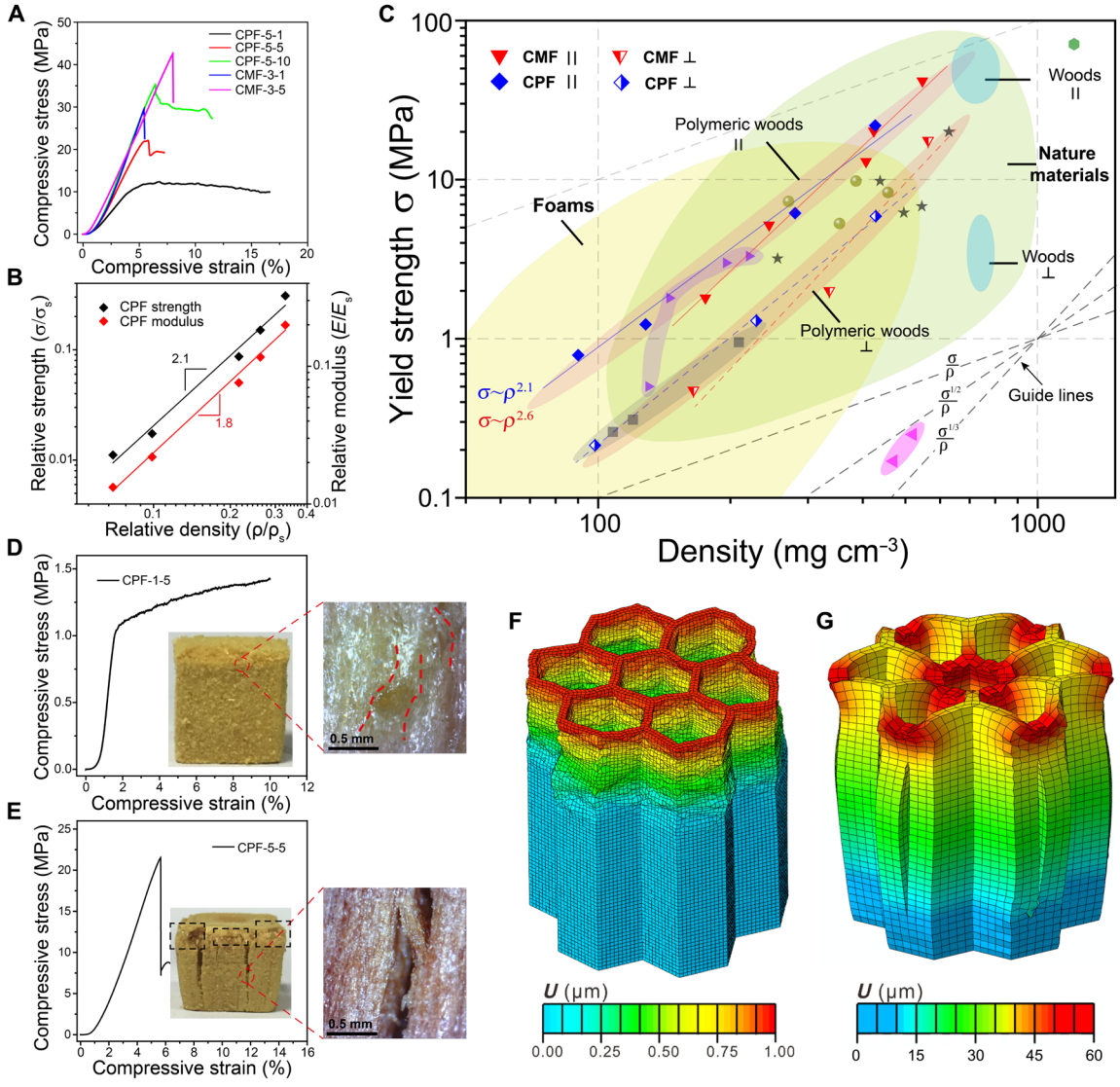

Fig. 3. Compressive performances and failure mechanisms of the polymeric woods. (**A**) Axial compressive stress-strain curves of typical polymeric woods. (**B**) Relative strength and modulus as functions of the relative density of CPF woods. (**C**) Ashby chart plotting compressive yield strength versus density for polymeric woods and other engineered materials, including cast resin ⬢ (*14*), SiC foam ▶ (*15*), 3D-printed honeycomb ★ (*14*), mullite-ZrO_2 foam ● (*16*), PF carbon foam ◀ (*24*), and RF aerogel ■ (*25*). Symbols ∥ and ⊥ represent the compressive directions that are parallel and perpendicular to the channels, respectively. (**D** and **E**) The compressive stress-strain curve, photograph, and micrographs show the bending-dominated failure of CPF-1-5 and the brittle cracking failure of CPF-5-5. The black boxes in (E) display the damage induced by the exfoliation of little blocks before the fracture appeared. (**F** and **G**) FEM simulations of thin- and thick-walled honeycomb structures for the low- and high-density polymeric woods. The honeycomb structures are colored by the total displacement of element nodes. (F) Bending-dominated wall buckling of thin-walled honeycomb structure. (G) Cracking failure of thick-walled honeycomb structure.

(fig. S19). In the axial compression of polymeric woods, we found two typical different failure modes, which depend on the resin (PF or MF) concentrations. The polymeric woods with relatively low densities, such as CPF-1-5 and CMF-1-5, deform through gradual plastic bending of cell walls and failure after reaching the yielding point (Fig. 3D, fig. S20, and movies S2 and S3) (*26*). The polymeric woods with high densities, such as CPF-5-5 and CMF-2-5, present apparent brittle fracture behaviors with a drastic drop of stress and an instantaneous cleaving of the structures (Fig. 3E, fig. S21, and movies S4 and S5). Obviously, there is an inherent relationship between the failure modes and the structural features induced by the polymer concentration in the preparation.

To shed light on the two different failure scenarios, we performed finite element method (FEM) simulations to understand the underlying deformation and damage mechanisms. In the FEM simulations, regular hexagonal hollow columns (honeycomb structure; fig. S22) were modeled to characterize the structural morphology of CPF and CMF specimens. As shown in Fig. 3F, the main failure of the thin-walled honeycomb structure is due to the bending-dominated buckling of thin walls (*27*), which is in good agreement with the compression experiment (fig. S20). It has been demonstrated that low polymer concentration resulted in thin walls and large pores. Therefore, compression directly caused bending and warping of thin walls near the honeycomb opening (pleated surface in the experiments). To simulate

the cracking failure of high-density polymeric woods, cohesive element generated closed crackles preexisting at the center of walls along the length direction. During the compression experiments of high-density specimens, at the beginning of failure (before the fracture appeared), the upper surface displayed damage with the exfoliation of little blocks (black boxes in Fig. 3E). This process led to the uneven contact surface (wall edges) in the compression. The exfoliation was mainly due to brittle thick-walled blocks and preparation-induced defects near the contact surface. On this basis, the model was modified with projecting parts at two symmetric edges (fig. S23). The walls with projecting parts appeared fractures in simulations, and then the cracking and further compression resulted in the obvious lateral expansion with lateral wall bending (Fig. 3G and fig. S23B). The mechanism of this cracking failure is similar to that of the classical Brazilian test of a cylinder (*28*), in which the compression-induced tensile stress pulls the cross section and then finally results in the fracture. For a similar model with thin walls, the deformation remained the bending and buckling of thin walls without wall cracking (fig. S24). Thus, the cracking failure mode should be attributed to the thick-walled honeycomb structure and the formed uneven contact surface in the compression. In addition, FEM simulations revealed that bending existed in both failure modes, that is, bending-dominated thin-walled buckling and cracking-induced lateral thick-walled bending, respectively. The bending deformations in the two failure modes were also in accordance with the scaling laws presented in Fig. 3B, demonstrating the bending-dominated plastic and cracking behaviors in structural failure. The insight obtained here would be useful for understanding the mechanical behavior of these wood-mimetic structural materials.

The bending performance of the polymeric woods was also evaluated. The flexural strengths of the polymeric woods (for example, CPF-5-5) bear comparison with those of the balsa woods. However, due to the inherent brittleness of thermoset resins, the polymeric woods (CPF-5-5) exhibit a slight toughness, with their flexural strain much lower than that of the natural balsa wood (fig. S25). Considering the difference between polymeric and balsa woods in structure and component, it is rational for the performance difference. Inspired by the unique microstructure of the natural wood, the toughness of the polymeric woods should be improved by compositing with biopolymers.

Corrosion resistance and thermal insulation

We then focus on corrosion resistance and thermal conductivity of the polymeric woods, which should demonstrate some potential applications in special environments. The natural woods have advantages in mechanical performances but usually suffer from some drawbacks, such as the poor corrosion resistance under unconventional conditions. Wooden architectures can potentially be destroyed by long-time corrosion of water due to the hydrophilia of the wood. To improve corrosion resistance, natural woods are always lacquered or treated by plasma and corona to create water repellency (*29*), resulting in high economic cost and additional complicated treatment. Here, corrosion resistance is an inherent advantage of the polymeric woods due to the natural inertness of PF and MF resins. CPF and CMF polymeric woods display hydrophobic surfaces, with contact angles of 120 to 150° in both the axial and radial directions, while balsa woods, with a contact angle of ~0°, quickly adsorb water (fig. S26). After immersing the polymeric woods into the pure water (pH 7) and sulfuric acid solution (pH 3) for 30 days, the compressive strengths and moduli in the axial direction scarcely decrease (Fig. 4A), whereas the compressive strengths of the two kinds of balsa wood (95 and 190 mg cm^{-3}) with the same treatment decrease to one-third of the original strengths and the moduli simultaneously decrease to ~60% (fig. S27).

Thermal conductivity is also an important performance index in engineering material evaluation. In constructional engineering, wooden structures generally manifest a better thermal insulation property than concrete structures due to the low thermal conductivity of wood (*30*). The thermal conductivity of balsa wood in the radial direction is ~40 mW m^{-1} K^{-1}, which is comparable to the expanded polystyrene (35 to 45 mW m^{-1} K^{-1}) and commercial PF foams (Fig. 4B) (*31*). However, their applications in the thermal insulated materials are extremely restricted by hydroscopicity, which would lead to the decreasing thermal resistance as moisture content increases (*32*). In our experiments, the polymeric woods, with a density similar to that of balsa woods (~90 mg cm^{-3}; for example, CPF-1-5), can achieve better thermal insulation with a thermal conductivity of 33 mW m^{-1} K^{-1} (Fig. 4B). In addition, compositing with nanomaterials into the cell walls can increase the interface thermal resistance, which benefits thermal insulations (*31*). For example, the CPF-1/GO-1 composite wood shows a reduced thermal conductivity (28.9 mW m^{-1} K^{-1}) compared with the pure CPF and CMF woods. We also found that the superinsulating composite wood could be prepared by further reducing the resol dosage. For example, the CPF/GO composite wood prepared by using half resol dosage of CPF-1/GO-1 (denoted CPF-0.5/GO-1) manifests a radial thermal conductivity of only 20.8 mW m^{-1} K^{-1}, greatly lower than that of the most common superinsulating criterion (25 mW m^{-1} K^{-1}) (Fig. 4B) (*33*).

The anisotropic structure with low density and high porosity was demonstrated to be beneficial to the thermal insulation (*34*, *35*). Four key characteristics are responsible for the superior thermal insulation. First, the thin walls and large pore channels reduce the solid thermal conduction of the walls in the radial direction (perpendicular to the pore direction). Second, the large pore channels (~50 μm) facilitate the anisotropic heat flow along the pore direction and reduce the proportion of the thermal conduction in the radial direction (Fig. 4C). Third, the closed nanopores in the walls, which are possibly induced by polycondensation, could further impede thermal conduction. Finally, the nanomaterials (such as GO layers) not only serve as thermal barriers to slow down the thermal transmission but also increase the interface, providing huge interfacial thermal resistance and greatly decreasing thermal conductivity (Fig. 4C) (*31*). Recently, it has been shown that natural wood–derived nanocellulose aerogels display a similar thermal insulation property with a thermal conductivity of as low as 28 mW m^{-1} K^{-1} (*34*). However, the nanosized spacing of the interfibril aggregate in the cellulose walls is mainly open pores, showing a limited contribution to the thermal insulation in the radial direction. Besides, it is a challenge to maintain low thermal conductivity for long time due to the high hydrophilia of CNFs.

Figure 4D shows polymeric woods, engineering materials, and many frequently used aerogel materials in the plane of thermal conductivity versus specific strength. Their outstanding thermal insulation and the excellent mechanical performance place this new class of polymeric woods among the state-of-the-art thermal insulators including the polymer/SiO_2 hybrid composite.

Fire resistance of the polymeric woods

Inflammability is a fatal weakness of natural wood; thus, inorganic coatings are always used to improve fire retardancy (*36*). Vertical

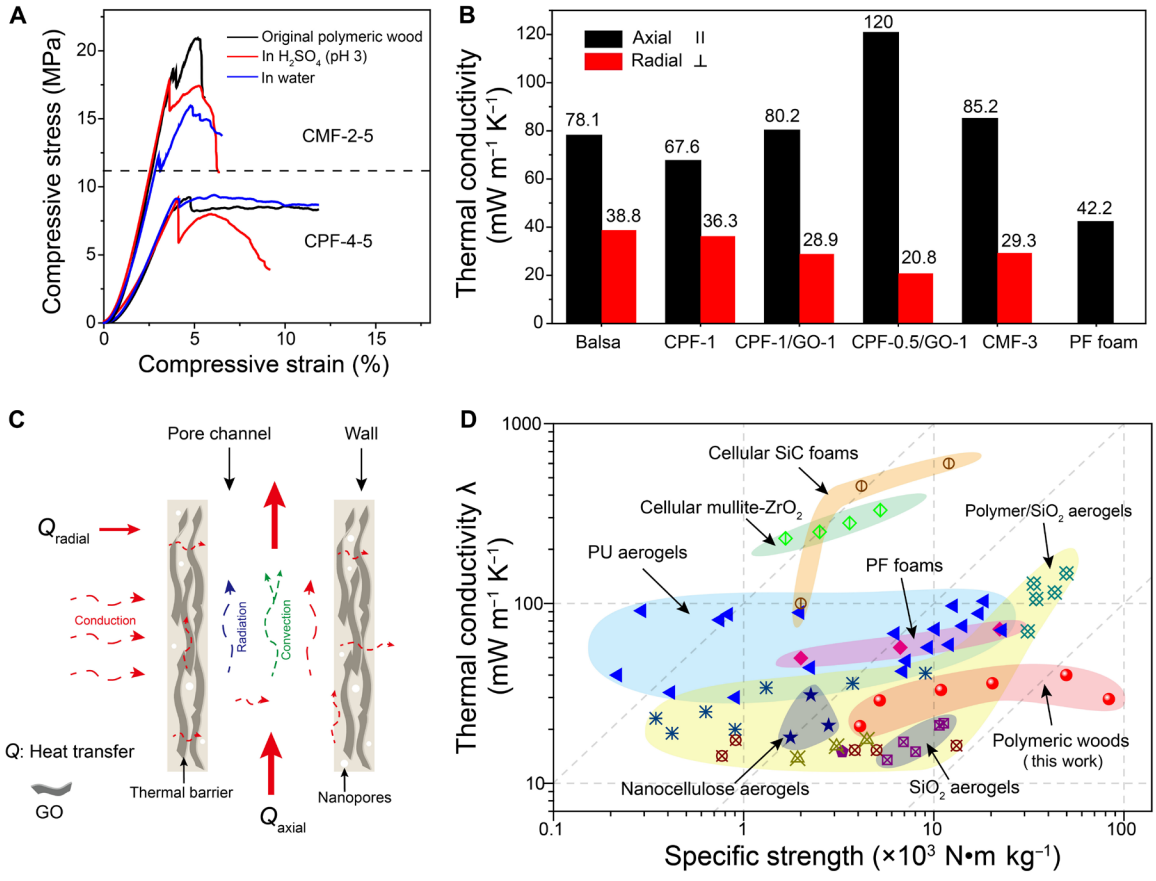

Fig. 4. Corrosion resistance and thermal conductivities of polymeric woods. (**A**) Axial compressive stress-strain curves of two typical polymeric woods before and after immersing in water or acid solution for 30 days. (**B**) Thermal conductivities of balsa, commercial PF foam, and polymeric woods. (**C**) Schematic illustration showing the difference of thermal conductivity in the radial and axial directions. (**D**) Thermal conductivity λ versus specific strength for ● polymeric woods, traditional aerogel-like materials, and other cellular ceramic materials, including polyurethane PU aerogels ◀ (*38*, *39*), PF foams ◆ (*40*), nanocellulose aerogels ★ (*41*), SiO_2 aerogels ⊠ (*42*), cellular CNF/GO/boric acid (BA)/sepiolite nanorods (SEP) aerogels ⬟ (*31*), SiC foams ⏀ (*15*), and mullite-ZrO_2 aerogels ◇ (*16*). The polymer/SiO_2 aerogels include pectin/SiO_2 aerogels ⊠ (*43*), cellulose/SiO_2 aerogels ⊠ (*44*), isocyanate/SiO_2 aerogels ✳ (*45*, *46*), and polyurethane/SiO_2 aerogels ⊠ (*47*).

burning test and limiting oxygen index (LOI) measurements were performed to examine fire retardancy of the polymeric woods (table S2). The polymeric woods display very good fire retardancy and self-extinguish quickly when removed from the igniting flame (fig. S28). The CPF/GO composite wood ignites with difficulty, while the balsa wood burned up quickly in combustion tests (movies S6 and S7). The lightweight CPF/SiC and CMF/SiC composite woods also burned because the SiC nanofibers restrain shrinkage and the low density allows contact of the materials with sufficient oxygen. The polymeric and composite woods exhibit a significantly higher LOI value than balsa wood (21%) and other commercial, flame retardant–containing polymer foams (*31*). As an extension for further possible applications, the performance of polymeric woods can be enhanced by compositing various nanomaterials, such as GO, SiC nanofibers, and sericite (Sc) nanosheets. Nanomaterials can inhibit shrinkage of the cryogels and result in a relatively narrow density range. The nanomaterials show almost no effect on axial compressive strength, but the compressive modulus is improved (fig. S29). The biggest difference between the composited wood and natural wood is oriented cellulose nanocrystal fibers along the pore direction (*37*). In addition, both the matrix resin and the inorganic nanomaterials are hard brittle materials, which could result in the premature failure of the entire structure due to insufficient toughness. While natural wood is a composite of semirigid lignin glue and rigid cellulose crystals, this natural "reinforced concrete structure" inspired us to seek somewhat flexible matrix materials, for example, polyurethane, amylopectin, sodium alginate, and other water-soluble resins. The flexible polymers and the oriented rigid nanofibers along the pore direction should yield outstanding artificial wood.

DISCUSSION

In summary, we have developed a simple strategy for large-scale fabrication of a family of artificial polymeric woods with controllable microstructures by a combined self-assembly and thermocuring process of the traditional resins. The polymeric and composite woods manifest outstanding comprehensive performance, including mechanical strength comparable to that of natural wood, better corrosion resistance to water and acid with no decrease in mechanical properties, as well as much better thermal insulation (as low as ~21 mW m^{-1} K^{-1}) and fire retardancy. The present polymeric woods even stand out from other engineering materials such as cellular

ceramic materials and aerogels in terms of specific strength and thermal insulation properties. As a kind of biomimetic engineering materials, this new family of bioinspired polymeric woods is supposed to replace the natural wood when used in harsh environments. This novel strategy provides a new and powerful route to fabricate and engineer a wide range of high-performance biomimetic engineering composite materials with desirable multifunctionality and advantages over the traditional counterparts, which will have broad applications in many technical fields.

MATERIALS AND METHODS

Fabrication of artificial polymeric woods (CPF and CMF)

In a typical synthesis, 0.60 g of phenol, 2.1 ml of formaldehyde solution (37 wt %), and 15 ml of (0.1 M) NaOH aqueous solution were mixed and stirred at 70°C for 1 hour. The pH of the light yellow viscous solution was adjusted to neutral by using diluted HCl, and water was removed with rotary evaporators (50 mbar, 50°C). Absolute ethyl alcohol (60 ml) was added, and then the mixture was filtrated to separate out the NaCl, followed by evaporating the ethanol to obtain the low–molecular weight phenolic resol. The resol was stored in freezer. CTS (2 g) and HAc (2 ml) were added to 100 ml of deionized water (DIW) under stirring to prepare the transparent and viscous CTS solution. Different masses of the resol (0.11 to 0.55 g) or MF (0.6 to 1.8 g) precursor were added to 3 ml of the CTS solution, followed by vibrating intensely and ultrasounding for 5 min. The fabrication details were listed in table S1. Then, the CTS/resin solution was poured into a mold that was put on a cold copper platform and unidirectionally frozen. The initial temperature of the cold platform was set to −10°C, and the freezing rate could be set to 1, 5, and 10°C min^{-1}. After freeze-drying in a freeze drier (Labconco-195), the polymeric cryogel was cured at different temperatures, such as 160°, 180°, and 200°C.

Preparation and modification of various nanomaterials

A Domsjö wood pulp with a solid content of ~30.3% was used as the cellulose source for the preparation of CNFs by TEMPO oxidation. Wood pulp (3.30 g; 1 g of dry cellulose) was suspended in 100 ml of water containing 0.016 g of 2,2,6,6-tetramethylpiperidine-1-oxyl (TEMPO) and 0.1 g of sodium bromide. Ten milliliters of 9% NaClO solution was adjusted to pH 10 by 0.5 M HCl, which was then added to the wood pulp suspension. The pH was maintained at 10 by adding 0.5 M NaOH until no NaOH consumption was observed. The TEMPO-oxidized pulp was then rinsed several times with DIW and suspended in DIW to form a pulp slurry. The TEMPO-oxidized pulp slurry was agitated for 5 min to obtain a transparent CNF dispersion.

The GO was prepared according to the modified Hummers' method. Briefly, 160 ml of sulfuric acid (98%) was added gently into a beaker containing 5.0 g of graphite and 3.75 g of $NaNO_3$ under stirring at room temperature. Subsequently, 20 g of $KMnO_4$ was gradually added over 40 min, and stirring was kept for 20 hours. After incubation for 6 days, 500 ml of DIW was added slowly under gentle agitation followed by the addition of 30 ml of H_2O_2 (30%). The product was centrifugally washed and shocked for several times. Finally, the brown dispersion was further purified by dialysis to completely remove the impurities.

SiC nanofibers were modified by coating a layer of RF by the Stöber method. The Sc nanosheets were modified by coating a layer of polydopamine (PDA). In a typical synthesis, 50 mg of Sc and 50 mg of tris were successively dissolved in 25 ml of DIW, and the pH was adjusted to 8.5 by diluted HCl. Dopamine hydrochloride (50 mg) was added to the above solution. After that, the solution was stirred for 12 hours in an open beaker. The obtained black Sc nanosheet was collected from the suspension through centrifugation and washed with water three times.

Fabrication of multifunctional composite woods

Different materials, such as metal ions [$FeCl_3$, $CoCl_2$, $NiCl_2$, and $Cr(NO_3)_3$, 0.2 mmol ml^{-1}], SiO_2 nanoparticles, CNFs, SiC@RF nanofiber, Sc@PDA nanosheets, and GO, were added to the polymer solution. The concentration of the nanomaterials could be 1, 5, and 10 mg ml^{-1}. All the composite woods are prepared at a freezing rate of 5°C min^{-1}, and the cryogels were cured at 180°C.

For example, the CPF-1/GO-1 composite wood was fabricated as follows. In a typical synthesis, 2.4 g of CTS and 2.4 ml of HAc were dispersed in 120 ml of GO solution (1 mg ml^{-1}) under stirring and ultrasound for 3 hours. Resol (4.4 g) was added to the above mixture solution under stirring to prepare the PF/GO solution. The solution was poured into a polydimethylsiloxane mold with an inner size of 5.6 cm × 5.6 cm × 4 cm, which was put on a precooled copper surface (−10°C). The solution was unidirectionally frozen at a freezing rate of 5°C min^{-1}. The frozen monolith was freeze-dried for 72 hours and then cured at 180°C for 1 hour.

The homemade equipment design and operation

To accurately control the freezing rate, a homemade equipment was designed according to a previous report (*11*). The equipment includes an automatic liquid nitrogen tank, frozen ethanol pool, sample stage (copper cylinder, diameter of 10 cm), and a temperature controller with a heating jacket wrapped the copper cylinder (fig. S4). Ethanol was used as a buffer of the liquid nitrogen due to its low melting point. The temperature controller can show the real-time temperature of the sample stage, maintain steady temperature, and control the freezing rate. Before the sample preparation, the temperature of the sample stage was maintained at −10°C. After adding the solution to the mold, the temperature of the sample stage was controlled to decrease at a constant rate. After the samples were completely frozen, the mold was taken down and the samples were taken out carefully. Note that any possible impact should be avoided, or else cracks will appear on the final samples.

Mechanical compression tests and computational simulation

Mechanical compression and bending tests were performed on an Instron 5565A universal testing machine equipped with two flat-surface compression stages and 5000-N load cells. FEM simulations were performed with the ABAQUS program. The sample size for the three-point bending test was 2 mm × 2 mm × 10 mm. The basic unit of the models was a regular hexagonal hollow column with a uniform wall thickness. The honeycomb structure could be obtained by repeating the basic unit. We used the thin- and thick-walled models to simulate the prepared materials (CMF and CPF) with low and high matrix concentrations, respectively. Although the hollow channels in the synthesized materials were irregular and inhomogeneous relatively, the honeycomb model could characterize the structural morphology from the perspective of theoretical simulation. In all simulations, the compression was realized by a rigid plane with a uniform displacement. The wall thickness of honeycomb structures and the pore area are

shown in fig. S11 and table S1. Preexisting crackles at the center of the walls along the length direction were generated by cohesive elements. The parameters of cohesive interface were referred to the experiment data of bulk materials. The low-density polymeric woods were first simulated by the thin-walled honeycomb structure (fig. S22). The step length of the displacement of rigid plate was 0.001 in all simulations. The large deflection effects were included in the solution of compression processes. Then, we used the thick-walled model with preexisting crackles (fig. S23) to simulate the high-density polymeric woods. Preexisting crackles were generated by cohesive elements. Because of our understanding of the cracking mechanism in the Brazilian test (*28*), we modified the thick-walled model with projecting parts at two symmetric edges. The similar thin-walled model was also simulated as a comparison (fig. S24). In FEM simulations, C3D8R and COH3D8 elements were selected for the walls and cohesive interfaces, respectively. Because of the limitations of computational cost and time, the meshing grids in thick-walled models with preexisting crackles were larger than those in thin-walled models. The wall thicknesses of the two models were 2.0 and 6.6 μm, respectively, and the side length of the hexagonal opening in both two models was 21 μm.

Characterization

SEM was performed with a field emission scanning electron microanalyzer (Zeiss Supra 40). All samples were gold-sputtered for 50 s at a constant current of 30 mA before observation. TEM was performed on H-7650 (Hitachi) operating at an acceleration voltage of 100 kV. The x-ray microtomography was conducted on Y.Cheetah (YXLON) for the 3D microstructural information. The raw data were reconstructed using the software VGStudio MAX 2.2 by assembling the static images in sequence. The skeletal densities of CPF and CMF were 1.3 ± 0.1 and 1 ± 0.1 g cm^{-3}, respectively, according to the pycnometer method. The in-site observation of the compressive process of polymeric woods was recorded with a monocular microscope (JT-1400B). The thermal conductivity was measured using the transient plane source technique. The vertical test was performed on a CFZ-2 type instrument (Jiangning Analysis Instrument Co.) according to the UL 94 test standard. The specimens used were of dimensions 130 mm × 13 mm × 3 mm. LOI was measured according to ASTM D2863. The apparatus used was an HC-2 oxygen index meter (Jiangning Analysis Instrument Co.). The specimens used for the test were of dimensions 100 mm × 6.5 mm × 3 mm.

Corrosion resistance tests

CPF-4-5, CMF-2-5, and balsa with a size of 1.5 cm × 1.5 cm × 1.5 cm were put in a beaker with pure water. The samples were floated spontaneously on the water surface and kept for 30 days. In another beaker, diluted sulfuric acid (pH 3) was used to examine the corrosion resistance of polymeric and balsa woods. At least three samples were tested for every sample. Then, the compressive performances of these woods were examined.

SUPPLEMENTARY MATERIALS

Supplementary material for this article is available at http://advances.sciencemag.org/cgi/content/full/4/8/eaat7223/DC1

Fig. S1. The chemical structures of matrix materials.
Fig. S2. SEM images of various MF-based composite woods.
Fig. S3. Large-scale fabrication of the polymeric wood.
Fig. S4. Photography of the homemade equipment to control the freezing rate.
Fig. S5. SEM images showing the changing trend of the microstructures of CPF woods with the increasing resol content and freezing rate, respectively.
Fig. S6. Statistical analysis of area distribution of the channels of CPF woods prepared at different freezing rates.
Fig. S7. Statistical analysis of wall thickness.
Fig. S8. SEM images showing the changing trend of the microstructures of CPF woods with the increasing resol content and curing temperature, respectively.
Fig. S9. Statistical analysis of area distribution of the channels of CPF woods prepared by using different curing temperatures.
Fig. S10. Statistical analysis of wall thickness.
Fig. S11. The averaged pore area and averaged wall thickness of CPF woods.
Fig. S12. SEM images of the CMF woods.
Fig. S13. Densities and porosities of the polymeric woods.
Fig. S14. The mechanical performances of CPF woods prepared at different freezing rates.
Fig. S15. The mechanical performances of CPF woods prepared at different curing temperatures.
Fig. S16. The mechanical performances of CMF woods prepared at different freezing rates.
Fig. S17. An Ashby chart plotting compressive stiffness versus density for CPF and CMF woods.
Fig. S18. The radial compression tests of balsa, CPF, and CMF woods.
Fig. S19. The axial compression of the balsa wood.
Fig. S20. The in situ micrographs show the failure of polymeric woods with relatively low density.
Fig. S21. The in situ micrographs show the failure of different polymeric woods with relatively high density.
Fig. S22. Thin-walled model for the compression simulations of low-density polymeric woods.
Fig. S23. The simulation models and results.
Fig. S24. A similar thin-walled model was also simulated as a comparison.
Fig. S25. Three-point bending test of balsa woods, polymeric woods, and a typical composite wood.
Fig. S26. The contact angles of the typical polymeric woods.
Fig. S27. The water resistance of balsa woods.
Fig. S28. The fire resistance of polymeric woods and balsa wood under an alcohol flame.
Fig. S29. The contrasts of CMF woods with various CMF-based composite woods in mechanical performance.
Table S1. The details of the synthesis of typical CPF and CMF woods and their respective parameters.
Table S2. Vertical burning test and LOI of the balsa (~300 mg cm^{-3}) and polymeric woods.
Movie S1. 3D observation of a typical CPF wood by x-ray microtomography.
Movie S2. The in situ observation of failure process of the low-density CPF-1-5 during the compression, revealing the gradual plastic bending of cell walls.
Movie S3. The in situ observation of failure process of the low-density CMF-1-5 during the compression, revealing the gradual plastic bending of cell walls.
Movie S4. The in situ observation of failure process of the high-density CPF-5-5 during the compression, revealing the brittle fracture behaviors.
Movie S5. The in situ observation of failure process of the high-density CMF-2-5 during the compression, revealing the brittle fracture behaviors.
Movie S6. The burning test of the CPF-1/GO-1 composite wood by using an alcohol lamp flame.
Movie S7. The burning test of the balsa wood by using an alcohol lamp flame.

REFERENCES AND NOTES

1. U. G. K. Wegst, H. Bai, E. Saiz, A. P. Tomsia, R. O. Ritchie, Bioinspired structural materials. *Nat. Mater.* **14**, 23–36 (2015).
2. H. D. Espinosa, R. Soler-Crespo, Materials science: Lessons from tooth enamel. *Nature* **543**, 42–43 (2017).
3. B. Yeom, T. Sain, N. Lacevic, D. Bukharina, S.-H. Cha, A. M. Waas, E. M. Arruda, N. A. Kotov, Abiotic tooth enamel. *Nature* **543**, 95–98 (2017).
4. E. Munch, M. E. Launey, D. H. Alsem, E. Saiz, A. P. Tomsia, R. O. Ritchie, Tough, bio-inspired hybrid materials. *Science* **322**, 1516–1520 (2008).
5. J. Aizenberg, P. Fratzl, Biological and biomimetic materials. *Adv. Mater.* **21**, 387–388 (2009).
6. P. Fratzl, F. G. Barth, Biomaterial systems for mechanosensing and actuation. *Nature* **462**, 442–448 (2009).
7. R. Weinkamer, P. Fratzl, Mechanical adaptation of biological materials—The examples of bone and wood. *Mater. Sci. Eng. C* **31**, 1164–1173 (2011).
8. J. Song, C. Chen, S. Zhu, M. Zhu, J. Dai, U. Ray, Y. Li, Y. Kuang, Y. Li, N. Quispe, Y. Yao, A. Gong, U. H. Leiste, H. A. Bruck, J. Y. Zhu, A. Vellore, H. Li, M. L. Minus, Z. Jia, A. Martini, T. Li, L. Hu, Processing bulk natural wood into a high-performance structural material. *Nature* **554**, 224–228 (2018).
9. C. Chen, J. Song, S. Zhu, Y. Li, Y. Kuang, J. Wan, D. Kirsch, L. Xu, Y. Wang, T. Gao, Y. Wang, H. Huang, W. Gan, A. Gong, T. Li, J. Xie, L. Hu, Scalable and sustainable approach toward highly compressible, anisotropic, lamellar carbon sponge. *Chem* **4**, 544–554 (2018).

10. R. Xiong, A. M. Grant, R. Ma, S. Zhang, V. V. Tsukruk, Naturally-derived biopolymer nanocomposites: Interfacial design, properties and emerging applications. *Mater. Sci. Eng. R Rep.* **125**, 1–41 (2018).
11. S. Deville, E. Saiz, R. K. Nalla, A. P. Tomsia, Freezing as a path to build complex composites. *Science* **311**, 515–518 (2006).
12. C. Minas, D. Carnelli, E. Tervoort, A. R. Studart, 3D printing of emulsions and foams into hierarchical porous ceramics. *Adv. Mater.* **28**, 9993–9999 (2016).
13. Z.-Z. Pan, H. Nishihara, S. Iwamura, T. Sekiguchi, A. Sato, A. Isogai, F. Kang, T. Kyotani, Q.-H. Yang, Cellulose nanofiber as a distinct structure-directing agent for xylem-like microhoneycomb monoliths by unidirectional freeze-drying. *ACS Nano* **10**, 10689–10697 (2016).
14. B. G. Compton, J. A. Lewis, 3D-printing of lightweight cellular composites. *Adv. Mater.* **26**, 5930–5935 (2014).
15. C. Ferraro, E. Garcia-Tuñon, V. G. Rocha, S. Barg, M. D. Fariñas, T. E. Gomez Alvarez-Arenas, G. Sernicola, F. Giuliani, E. Saiz, Light and strong SiC networks. *Adv. Funct. Mater.* **26**, 1636–1645 (2016).
16. M. Fukushima, Y.-i. Yoshizawa, Fabrication of highly porous honeycomb-shaped mullite–zirconia insulators by gelation freezing. *Adv. Powder Technol.* **27**, 908–913 (2016).
17. M. A. Meyers, P.-Y. Chen, A. Y.-M. Lin, Y. Seki, Biological materials: Structure and mechanical properties. *Prog. Mater. Sci.* **53**, 1–206 (2008).
18. Z.-L. Yu, Z.-Y. Wu, S. Xin, C. Qiao, Z.-Y. Yu, H.-P. Cong, S.-H. Yu, General and straightforward synthetic route to phenolic resin gels templated by chitosan networks. *Chem. Mater.* **26**, 6915–6918 (2014).
19. H. Zhang, J. Long, A. I. Cooper, Aligned porous materials by directional freezing of solutions in liquid CO_2. *J. Am. Chem. Soc.* **127**, 13482–13483 (2005).
20. M. C. Gutiérrez, M. L. Ferrer, F. del Monte, Ice-templated materials: Sophisticated structures exhibiting enhanced functionalities obtained after unidirectional freezing and ice-segregation-induced self-assembly. *Chem. Mater.* **20**, 634–648 (2008).
21. S. Deville, Freeze-casting of porous biomaterials: Structure, properties and opportunities. *Materials* **3**, 1913–1927 (2010).
22. X. Zheng, H. Lee, T. H. Weisgraber, M. Shusteff, J. DeOtte, E. B. Duoss, J. D. Kuntz, M. M. Biener, Q. Ge, J. A. Jackson, S. O. Kucheyev, N. X. Fang, C. M. Spadaccini, Ultralight, ultrastiff mechanical metamaterials. *Science* **344**, 1373–1377 (2014).
23. L. J. Gibson, M. F. Ashby, *Cellular Solids: Structure and Properties* (Cambridge Univ. Press, 2001).
24. G. Nam, S. Choi, H. Byun, Y.-M. Rhym, S. E. Shim, Preparation of macroporous carbon foams using a polyurethane foam template replica method without curing step. *Macromol. Res.* **21**, 958–964 (2013).
25. G. Hasegawa, T. Shimizu, K. Kanamori, A. Maeno, H. Kaji, K. Nakanishi, Highly flexible hybrid polymer aerogels and xerogels based on resorcinol-formaldehyde with enhanced elastic stiffness and recoverability: Insights into the origin of their mechanical properties. *Chem. Mater.* **29**, 2122–2134 (2017).
26. L. J. Gibson, Modelling the mechanical behavior of cellular materials. *Mater. Sci. Eng. A* **110**, 1–36 (1989).
27. L. Aktay, A. F. Johnson, B.-H. Kröplin, Numerical modelling of honeycomb core crush behaviour. *Eng. Fract. Mech.* **75**, 2616–2630 (2008).
28. J. A. Hudson, Tensile strength and the ring test, *Int. J. Rock. Mech. Min. Sci. Geomech. Abstr.* **6**, 91–97 (1969).
29. L. Podgorski, B. Chevet, L. Onic, A. Merlin, Modification of wood wettability by plasma and corona treatments. *Int. J. Adhes. Adhes.* **20**, 103–111 (2000).
30. B. M. Suleiman, J. Larfeldt, B. Leckner, M. Gustavsson, Thermal conductivity and diffusivity of wood. *Wood Sci. Technol.* **33**, 465–473 (1999).
31. B. Wicklein, A. Kocjan, G. Salazar-Alvarez, F. Carosio, G. Camino, M. Antonietti, L. Bergström, Thermally insulating and fire-retardant lightweight anisotropic foams based on nanocellulose and graphene oxide. *Nat. Nanotechnol.* **10**, 277–283 (2015).
32. F. Ochs, W. Heidemann, H. Müller-Steinhagen, Effective thermal conductivity of moistened insulation materials as a function of temperature. *Int. J. Heat Mass Transfer* **51**, 539–552 (2008).
33. M. Koebel, A. Rigacci, P. Achard, Aerogel-based thermal superinsulation: An overview. *J. Sol-Gel Sci. Technol.* **63**, 315–339 (2012).
34. J. Song, C. Chen, Z. Yang, Y. Kuang, T. Li, Y. Li, H. Huang, I. Kierzewski, B. Liu, S. He, T. Gao, S. U. Yuruker, A. Gong, B. Yang, L. Hu, Highly compressible, anisotropic aerogel with aligned cellulose nanofibers. *ACS Nano* **12**, 140–147 (2018).
35. T. Li, J. Song, X. Zhao, Z. Yang, G. Pastel, S. Xu, C. Jia, J. Dai, C. Chen, A. Gong, F. Jiang, Y. Yao, T. Fan, B. Yang, L. Wågberg, R. Yang, L. Hu, Anisotropic, lightweight, strong, and super thermally insulating nanowood with naturally aligned nanocellulose. *Sci. Adv.* **4**, eaar3724 (2018).
36. T. Harada, Y. Nakashima, Y. Anazawa, The effect of ceramic coating of fire-retardant wood on combustibility and weatherability. *J. Wood Sci.* **53**, 249–254 (2007).
37. F. Barthelat, Z. Yin, M. J. Buehler, Structure and mechanics of interfaces in biological materials. *Nat. Rev. Mater.* **1**, 16007 (2016).
38. C. Chidambareswarapattar, P. M. McCarver, H. Luo, H. Lu, C. Sotiriou-Leventis, N. Leventis, Fractal multiscale nanoporous polyurethanes: Flexible to extremely rigid aerogels from multifunctional small molecules. *Chem. Mater.* **25**, 3205–3224 (2013).
39. N. Diascorn, S. Calas, H. Sallée, P. Achard, A. Rigacci, Polyurethane aerogels synthesis for thermal insulation—textural, thermal and mechanical properties. *J. Supercrit. Fluids* **106**, 76–84 (2015).
40. G. de Carvalho, J. A. Pimenta, W. N. dos Santos, E. Frollini, Phenolic and lignophenolic closed cells foams: Thermal conductivity and other properties. *Polym. Plast. Technol. Eng.* **42**, 605–626 (2003).
41. Y. Kobayashi, T. Saito, A. Isogai, Aerogels with 3D ordered nanofiber skeletons of liquid-crystalline nanocellulose derivatives as tough and transparent insulators. *Angew. Chem. Int. Ed.* **53**, 10394–10397 (2014).
42. J. C. H. Wong, H. Kaymak, S. Brunner, M. M. Koebel, Mechanical properties of monolithic silica aerogels made from polyethoxydisiloxanes. *Microporous Mesoporous Mater.* **183**, 23–29 (2014).
43. S. Zhao, W. J. Malfait, A. Demilecamps, Y. Zhang, S. Brunner, L. Huber, P. Tingaut, A. Rigacci, T. Budtova, M. M. Koebel, Strong, thermally superinsulating biopolymer-silica aerogel hybrids by cogelation of silicic acid with pectin. *Angew. Chem. Int. Ed.* **54**, 14282–14286 (2015).
44. S. Zhao, Z. Zhang, G. Sèbe, R. Wu, R. V. Rivera Virtudazo, P. Tingaut, M. M. Koebel, Multiscale assembly of superinsulating silica aerogels within silylated nanocellulosic scaffolds: Improved mechanical properties promoted by nanoscale chemical compatibilization. *Adv. Funct. Mater.* **25**, 2326–2334 (2015).
45. A. Katti, N. Shimpi, S. Roy, H. Lu, E. F. Fabrizio, A. Dass, L. A. Capadona, N. Leventis, Chemical, physical, and mechanical characterization of isocyanate cross-linked amine-modified silica aerogels. *Chem. Mater.* **18**, 285–296 (2006).
46. M. A. B. Meador, L. A. Capadona, L. McCorkle, D. S. Papadopoulos, N. Leventis, Structure–property relationships in porous 3D nanostructures as a function of preparation conditions: Isocyanate cross-linked silica aerogels. *Chem. Mater.* **19**, 2247–2260 (2007).
47. G. Churu, B. Zupančič, D. Mohite, C. Wisner, H. Luo, I. Emri, C. Sotiriou-Leventis, N. Leventis, H. Lu, Synthesis and mechanical characterization of mechanically strong, polyurea-crosslinked, ordered mesoporous silica aerogels. *J. Sol-Gel Sci. Technol.* **75**, 98–123 (2015).

Acknowledgments

Funding: This work was supported by the National Natural Science Foundation of China (grants 51732011 and 11525211), the Foundation for Innovative Research Groups of the National Natural Science Foundation of China (grant 21521001), Key Research Program of Frontier Sciences, Chinese Academy of Sciences (grant QYZDJ-SSW-SLH036), the Strategic Priority Research Program of the Chinese Academy of Sciences (XDB22040402), the National Basic Research Program of China (grant 2014CB931800), the Fundamental Research Funds for the Central Universities (WK2090050040), and the Users with Excellence and Scientific Research Grant of Hefei Science Center of Chinese Academy of Sciences (2015HSC-UE007). Z.-L.Y. acknowledges the funding support from the National Postdoctoral Program for Innovative Talents (grant BX201700220) and the China Postdoctoral Science Foundation (2017M622017). Y.-B.Z. acknowledges the funding support from the National Postdoctoral Program for Innovative Talents (grant BX201700225). This work was partially carried out at the University of Science and Technology of China Center for Micro and Nanoscale Research and Fabrication. **Author contributions:** S.-H.Y., Z.-L.Y., and N.Y. designed the experiments. Z.-L.Y., N.Y., Z.-Y.M., and B.Q. carried out the synthetic experiment and analysis. T.M. and S.-C.L. helped in the synthesis of the composite woods. L.-C.Z., Y.-B.Z., and H.-A.W. processed the FEM simulations and mechanical analysis. Y.-Y.L. and H.-L.G. conducted the 3D reconstruction of the structure. W.-Y.X. performed the fire-retardant experiments. S.-H.Y. and Z.-L.Y. wrote the paper. All authors discussed the results and commented on the manuscript. **Competing interests:** The authors declare that they have no competing interests. **Data and materials availability:** All data needed to evaluate the conclusions in the paper are present in the paper and/or the Supplementary Materials. Additional data related to this paper may be requested from the authors.

Submitted 28 March 2018
Accepted 29 June 2018
Published 10 August 2018
10.1126/sciadv.aat7223

Citation: Z.-L. Yu, N. Yang, L.-C. Zhou, Z.-Y. Ma, Y.-B. Zhu, Y.-Y. Lu, B. Qin, W.-Y. Xing, T. Ma, S.-C. Li, H.-L. Gao, H.-A. Wu, S.-H. Yu, Bioinspired polymeric woods. *Sci. Adv.* **4**, eaat7223 (2018).

ScienceAdvances

Bioinspired polymeric woods

Zhi-Long Yu, Ning Yang, Li-Chuan Zhou, Zhi-Yuan Ma, Yin-Bo Zhu, Yu-Yang Lu, Bing Qin, Wei-Yi Xing, Tao Ma, Si-Cheng Li, Huai-Ling Gao, Heng-An Wu, and Shu-Hong Yu

Sci. Adv. **4** (8), eaat7223. DOI: 10.1126/sciadv.aat7223